

faults. We have demonstrated this phenomenon in a friction-based fault model, but the overall dynamics of the process should be similar for viscoplastic deeper fault extensions, which may dynamically localize and weaken due to shear-heating and strain-rate effects during large earthquakes (19) and maintain their localization through the interseismic period because of the resulting structural differences in terms of their grain size and heterogeneity (31). Our study has focused on major strike-slip faults, but it has important relevance for the seismic hazard of megathrust subduction zones that are seismically quiescent, such as the Cascadia subduction zone, given the critical effect of down-dip rupture limit on coastal shaking.

REFERENCES AND NOTES

- C. H. Scholz, *The Mechanics of Earthquakes and Faulting* (Cambridge Univ. Press, New York, ed. 2, 2002).
- F. M. Chester, J. S. Chester, *Tectonophysics* **295**, 199–221 (1998).
- D. R. Shelly, *Nature* **463**, 648–652 (2010).
- R. E. Rellinger *et al.*, *Science* **289**, 1519–1524 (2000).
- J. Cole *et al.*, *J. Geophys. Res. Solid Earth* **112**, B12304 (2007).
- F. Waldhauser, W. L. Ellsworth, D. P. Schaff, A. Cole, *Geophys. Res. Lett.* **31**, L18608 (2004).
- E. Hauksson, W. Yang, P. M. Shearer, *Bull. Seismol. Soc. Am.* **102**, 2239–2244 (2012).
- N. Lapusta, J. R. Rice, *J. Geophys. Res. Solid Earth* **108**, 2205 (2003).
- P. M. Mai, K. K. S. Thingbaijam, *Seismol. Res. Lett.* **85**, 1348–1357 (2014).
- Supplementary materials are available on Science Online.
- Y. Fialko, *Nature* **441**, 968–971 (2006).
- A. Lin *et al.*, *Tectonophysics* **402**, 21–35 (2005).
- T. Shimamoto, *J. Struct. Geol.* **11**, 51–64 (1989).
- B. E. Shaw, S. G. Wesnousky, *Bull. Seismol. Soc. Am.* **98**, 1633–1641 (2008).
- J. Dieterich, in *Treatise on Geophysics*, G. Schubert, Ed. (Elsevier, Oxford, ed. 2, 2007), vol. 4, pp. 93–110.
- S. Barbot, N. Lapusta, J.-P. Avouac, *Science* **336**, 707–710 (2012).
- G. Di Toro *et al.*, *Nature* **471**, 494–498 (2011).
- J. R. Rice, *J. Geophys. Res.* **111**, B05311 (2006).
- J. D. Platt, J. W. Rudnicki, J. R. Rice, *J. Geophys. Res. Solid Earth* **119**, 4334–4359 (2014).
- H. Noda, N. Lapusta, *Nature* **493**, 518–521 (2013).
- R. H. Sibson, *Nature* **243**, 66–68 (1973).
- P. Segall, A. M. Bradley, *J. Appl. Mech.* **79**, 031013 (2012).
- G. Hirth, N. M. Beeler, *Geology* **43**, 223–226 (2015).
- J. C. Savage, *J. Geophys. Res.* **111**, B04405 (2006).
- M. Bouchon, H. Karabulut, *Science* **320**, 1323–1325 (2008).
- K. E. Sieh, *Bull. Seismol. Soc. Am.* **68**, 1421–1434 (1978).
- O. Zielke, J. R. Arrowsmith, L. G. Ludwig, S. O. Akçiz, *Science* **327**, 1119–1122 (2010).
- B. R. Smith-Konter, D. T. Sandwell, P. M. Shearer, *J. Geophys. Res.* **116**, B06401 (2011).
- L. B. Grant, A. Donnellan, *Bull. Seismol. Soc. Am.* **84**, 241–246 (1994).
- E. E. Runnerstrom, L. B. Grant, J. R. Arrowsmith, D. D. Rhodes, E. M. Stone, *Bull. Seismol. Soc. Am.* **92**, 2659–2669 (2002).
- P. B. Kelemen, G. Hirth, *Nature* **446**, 787–790 (2007).
- G. C. Beroza, *Bull. Seismol. Soc. Am.* **81**, 1603–1621 (1991).
- J. L. Elliott, J. T. Freymueller, B. Rabus, *J. Geophys. Res.* **112**, B06421 (2007).

ACKNOWLEDGMENTS

This study was supported by the U.S. Geological Survey (USGS) (grant G14AP00033), the National Science Foundation (NSF) (grants EAR 1142183 and 1520907), and the Southern California Earthquake Center (SCEC, funded by NSF cooperative agreement EAR-0529922 and USGS Cooperative agreement 07HQAG0008). This is SCEC contribution no. 6139. Numerical simulations for this study were carried out on the CITerra Dell cluster at the Division of Geological and Planetary Sciences of the California Institute of Technology. We thank J.-P. Ampuero, J.-P. Avouac, E. Hauksson,

and M. Simons for helpful discussions and comments on the manuscript. Earthquake catalogs and fault-slip models are compiled from published literature and publicly available sources. Numerical data are available from the authors upon request.

SUPPLEMENTARY MATERIALS

www.sciencemag.org/content/352/6291/1293/suppl/DC1
Materials and Methods

Supplementary Text
Figs. S1 to S21
Tables S1 to S3
Movies S1 and S2
References (34–117)

27 December 2015; accepted 11 May 2016
10.1126/science.aaf1496

QUANTUM SIMULATION

Quantum spin dynamics and entanglement generation with hundreds of trapped ions

Justin G. Bohnet,^{1*} Brian C. Sawyer,^{1,2} Joseph W. Britton,^{1,3} Michael L. Wall,⁴ Ana Maria Rey,⁵ Michael Foss-Feig,^{3,6} John J. Bollinger^{1*}

Quantum simulation of spin models can provide insight into problems that are difficult or impossible to study with classical computers. Trapped ions are an established platform for quantum simulation, but only systems with fewer than 20 ions have demonstrated quantum correlations. We studied quantum spin dynamics arising from an engineered, homogeneous Ising interaction in a two-dimensional array of ⁹Be⁺ ions in a Penning trap. We verified entanglement in spin-squeezed states of up to 219 ions, directly observing 4.0 ± 0.9 decibels of spectroscopic enhancement, and observed states with non-Gaussian statistics consistent with oversqueezed states. The good agreement with ab initio theory that includes interactions and decoherence lays the groundwork for simulations of the transverse-field Ising model with variable-range interactions, which are generally intractable with classical methods.

Quantum simulation, in which a well-controlled quantum system emulates another system to be studied, can be used to address classically intractable problems in fields including condensed-matter and high-energy physics, cosmology, and chemistry (1–3). Of particular interest are simulations of the transverse-field Ising spin model (4), described by the Hamiltonian

$$\hat{H}_T = \hat{H}_I + \hat{H}_B \quad (1)$$

$$\hat{H}_I = \frac{1}{N} \sum_{i < j} J_{ij} \hat{\sigma}_i^z \hat{\sigma}_j^z, \hat{H}_B = \sum_i B_x \hat{\sigma}_i^x \quad (2)$$

where N is the number of spins, J_{ij} parameterizes the spin-spin interaction, B_x parameterizes a transverse magnetic field, and $\hat{\sigma}_i^z$, $\hat{\sigma}_i^x$ are Pauli spin matrices. A quantum simulation of \hat{H}_T could illuminate complex phenomena in quantum magnetism, including quantum phase transitions, many-body localization, and glassiness in spin systems (5–8), and clarify whether quantum an-

nealing can provide an advantage for solving hard optimization problems (9, 10).

Ensembles of photons, ions, neutral atoms, molecules, and superconducting circuits are all being developed as quantum simulation platforms (3). A variety of quantum spin models have been realized with large ensembles of neutral atoms (11–15) and molecules (16). Trapped-ion quantum simulators can implement \hat{H}_T (17–19) and have a number of advantages over other implementations, such as high-fidelity state preparation and readout, long trapping and coherence times, and strong, variable-range spin-spin couplings. To date, trapped-ion simulators have been constrained to systems of about 20 spins (18, 20), for which classical numerical simulations remain tractable; substantial engineering efforts are under way to increase the number of ions by cryogenically cooling linear traps and two-dimensional (2D) surface-electrode traps (21, 22).

Penning traps have emerged as a viable option for performing quantum simulations with hundreds of ions (23–26). Laser-cooled ions in a Penning trap self-assemble into 2D triangular lattices and are amenable to similar high-fidelity spin-state control, long trapping times, and generation of transverse-field Ising interactions as ions in linear Paul traps. Previous work in Penning traps demonstrated control of the collective spin (27) and benchmarked the engineered, variable-range Ising interaction in the mean-field, semiclassical limit (24–26). However, for a simulator of quantum magnetism to be trusted, quantum

¹National Institute of Standards and Technology (NIST), Boulder, CO 80305, USA. ²Georgia Tech Research Institute, Atlanta, GA 30332, USA. ³Army Research Lab, Adelphi, MD 20783, USA. ⁴JILA, NIST, and University of Colorado, Boulder, CO 80309, USA. ⁵JILA, NIST, and Department of Physics, University of Colorado, Boulder, CO 80309, USA. ⁶Joint Quantum Institute and NIST, Gaithersburg, MD 20899, USA. *Corresponding author. Email: justin.bohnet@nist.gov (J.G.B.); jib@nist.gov (J.J.B.)

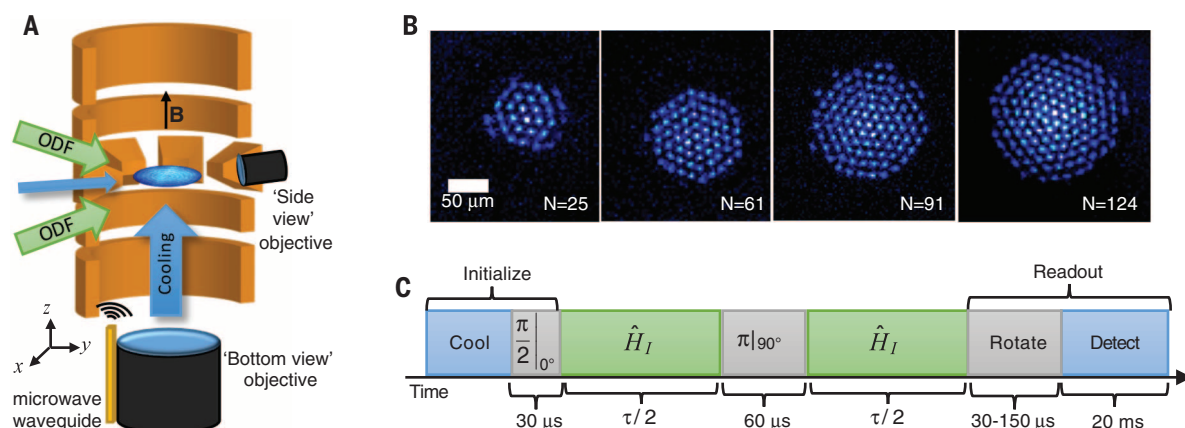


Fig. 1. Penning trap quantum simulator. (A) A cross-sectional illustration of the Penning trap (not to scale). The orange electrodes provide axial confinement and the rotating wall potential. The 4.5 T magnetic field is directed along the z axis. The blue disk indicates the 2D ion crystal. Resonant Doppler cooling is performed with the beams along z and y . The spin state-dependent optical dipole force (ODF) beams enter $\pm 10^\circ$ from the 2D ion plane. Resonant microwave radiation for coupling ground states $|\uparrow\rangle$ and $|\downarrow\rangle$ is delivered through a waveguide. State-dependent fluorescence is collected through the pair of imaging objectives, where the bright state corresponds to $|\uparrow\rangle$. (B) Coulomb crystal

images in a frame rotating at ω_r with ${}^9\text{Be}^+$ ions in $|\uparrow\rangle$, with the number of ions N indicated. (C) The typical experiment pulse sequence, composed of cooling laser pulses (blue), microwave pulses (gray), and ODF laser pulses (green). Cooling and repumping initialize each ion in $|\uparrow\rangle$, and then a microwave $\pi/2$ pulse prepares the spins along the x axis. Suddenly switching on \hat{H}_I initiates the non-equilibrium spin dynamics. The microwave π pulse implements a spin echo, reducing dephasing from magnetic field fluctuations and ODF laser light shifts. State readout consists of a final global rotation and fluorescence detection. The final microwave pulse area and phase are chosen to measure the desired spin projection.

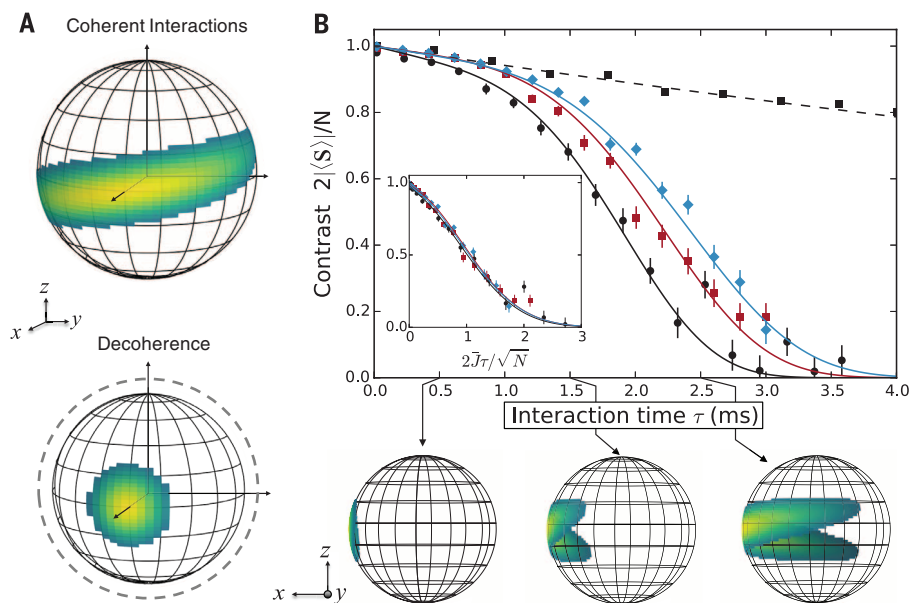


Fig. 2. Depolarization of the collective spin from spin-spin interactions and decoherence. (A) The Husimi distribution of the collective spin state on a Bloch sphere calculated for the experimental parameters in (B), with $N = 21$, illustrating (top) an oversqueezed state generated by the Ising interaction at time $\tau = 2$ ms with no decoherence and (bottom) a loss of contrast only from decoherence, effectively shrinking the Bloch sphere. (B) Contrast versus interaction time for $N = 21$, 58, and 144 ions indicated by black circles, red squares, and blue diamonds, respectively. Data are means \pm SD; the solid lines are predictions, with no free parameters, from a model that includes decoherence from spontaneous emission (28). The contrast decay from decoherence caused by spontaneous emission is measured in the absence of spin-spin coupling (black squares with the dashed line showing an exponential fit). At each τ , the detuning δ is adjusted to eliminate spin-motion coupling at the end of the experiment, resulting in a different $\bar{J} \propto 1/\delta$ for each point. The Bloch spheres show the Husimi distribution for a pure state of $N = 21$ at three different interaction times, ignoring the effects of decoherence. Inset: The data collapse to a common curve with proper rescaling, indicating that the depolarization is dominated by coherent spin-spin interactions.

correlations generated by the Ising interaction must be observed and understood. For large trapped-ion simulators, this benchmarking requires a detailed accounting of many-body physics in an open quantum system.

Here, we observed and benchmarked entanglement in hundreds of trapped ions generated with engineered Ising interactions in a 2D array of ${}^9\text{Be}^+$ ions in a Penning trap. To enable efficient theoretical computation of the spin dynamics (28), we performed experiments with a homogeneous Ising interaction and without simultaneous application of the transverse field B_x , finding good agreement with a solution of the full quantum master equation.

Our experimental system consists of between 20 and 300 ${}^9\text{Be}^+$ ions confined to a single-plane Coulomb crystal in a Penning trap (Fig. 1) (28). The trap is characterized by an axial magnetic field $|\mathbf{B}| = 4.45$ T and an axial trap frequency $\omega_z = 2\pi \times 1.57$ MHz. A stack of cylindrical electrodes generates a harmonic confining potential along their axis. Radial confinement is provided by the Lorentz force from $\mathbf{E} \times \mathbf{B}$ -induced rotation in the axial magnetic field. Time varying potentials applied to eight azimuthally segmented electrodes generate a rotating wall potential that controls the crystal rotation frequency ω_r , typically between $2\pi \times 172$ kHz and $2\pi \times 190$ kHz.

The spin- $1/2$ system is the ${}^2S_{1/2}$ ground state of the valence electron spin $|\uparrow\rangle \equiv |m_s\rangle = +1/2$, $|\downarrow\rangle \equiv |m_s\rangle = -1/2$. In the magnetic field of the Penning trap, the ground state is split by 124 GHz. A resonant microwave source provides an effective transverse field, which we use to perform global rotations of the spin ensemble with a Rabi frequency of 8.3 kHz. The T_2 spin echo coherence

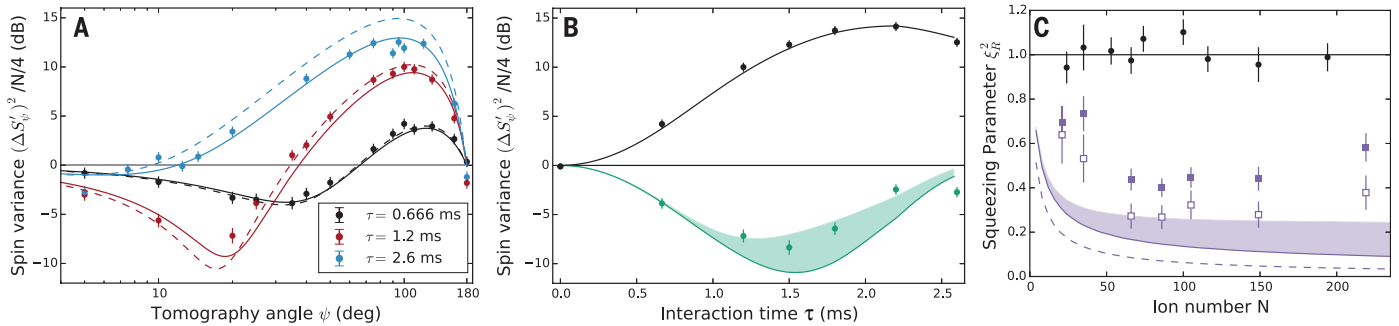


Fig. 3. Spin variance and entanglement. (A) Spin variance (symbols) as a function of tomography angle ψ for $N = 86 \pm 2$. The variance is calculated from 200 trials. The solid lines are a prediction, with no free parameters, assuming homogeneous Ising interactions and including decoherence from spontaneous emission (28). The dashed lines are theoretical predictions with the same interaction parameters but no decoherence. (B) The explicit time dependence of the spin variance for the ensemble in (A). The data for the minimum (green points) and maximum (black points) spin variance are shown with theory predictions of the optimal squeezing and antisqueezing (solid lines), including decoherence. Because our measurement of $(\Delta S_\psi)^2$ has substantial granularity, we visualize the effect of finite sampling of ψ on the measured minimum variance using the green shaded region bounded by $\max\{[(\Delta S_\psi(\psi_m \pm 5^\circ))^2]\}$, where ψ_m corresponds

to the angle that minimizes $(\Delta S_\psi)^2$. The $\pm 5^\circ$ uncertainty does not have a visible effect in the squeezed component for short times, or for the antisqueezing component at any time. (C) Ramsey squeezing parameter measured for different ensemble sizes N . The black points show data for the initial unentangled spin state. The solid purple squares show the lowest directly measured ξ_R^2 with no corrections or subtractions of any detection noise for evaluation of the entanglement witness. The open squares show ξ_R^2 inferred by subtracting photon shot noise. The dashed line is the predicted optimal ξ_R^2 from coherent Ising interactions with no decoherence, and the solid line shows the limit including spontaneous emission assuming $\Gamma/J = 0.05$, which is typical for our system. The shaded purple region accounts for finite sampling of ψ as in (B). All error bars denote SE.

time is 15 ms. Optical transitions to the $^2P_{3/2}$ states are used for state preparation, Doppler cooling, and projective measurement (28).

The Ising interaction is implemented by a spin-dependent optical dipole force (ODF) generated from the interference of a pair of detuned lasers (Fig. 1A). The ODF couples the spin and motional degrees of freedom through the interaction

$$\hat{H}_{\text{ODF}} = \sum_{i=1}^N F_0 \cos(\mu t) \hat{z}_i \hat{\sigma}_i^z \quad (3)$$

where \hat{z}_i is the position operator for ion i , $\mu/2\pi$ is the ODF laser beat frequency, and F_0 is the force amplitude, typically 30 nN. The ODF drives the axial drumhead modes of the planar ion crystal (25, 26), generating an effective spin-spin interaction by modifying the ions' Coulomb potential energy (29). Detuning μ from ω_z changes the effective range of the spin-spin interaction $J_{i,j} \propto d_{i,j}^{-a}$, where $d_{i,j}$ is the ion separation. Although a can range from 0 to 3 (24), in this work we primarily drive the highest-frequency, center-of-mass (COM) mode at ω_z with ODF detunings $\delta = \mu - \omega_z$ ranging from about $2\pi \times 0.5$ kHz to $2\pi \times 3$ kHz, such that a varies from 0.02 to 0.18, respectively. The next closest axial motional mode frequency is more than $2\pi \times 20$ kHz lower than ω_z . Because $a \ll 1$, the Ising interaction is approximately independent of distance, resulting in a homogeneous pairwise coupling $J_{i,j} \approx \bar{J} = F_0^2/(4M\omega_z\delta)$, where M is the ion mass.

At the mean-field level, each spin precesses in an effective magnetic field determined by the couplings to other spins, described by the Hamiltonian

$$\hat{H}_{\text{MF}} = \sum_{j=1}^N \frac{\bar{B}_j \hat{\sigma}_j^z}{2} \quad (4)$$

where

$$\bar{B}_j = \frac{2}{N} \sum_{i \neq j} J_{i,j} \langle \hat{\sigma}_i^z \rangle \quad (5)$$

We calibrated \bar{J} through measurements of mean-field spin precession (24, 28), typically finding $\bar{J}/\hbar \leq 3300$ s $^{-1}$. For the experiments described below, we started with all the spins initialized in an eigenstate of $\hat{\sigma}^x$ so that $\bar{B}_j = 0$. This choice of initial condition ensured that the observed physics are dominated by quantum correlations and decoherence alone.

State readout was performed using fluorescence from the Doppler cooling laser on the cycling transition (28). Ions in $|\uparrow\rangle$ fluoresce and ions in $|\downarrow\rangle$ are dark. Global fluorescence was collected with the side-view objective (Fig. 1A) and counted with a photomultiplier tube. We used the bottom-view image to count the number of ions and thereby calibrate the photon counts per ion (Fig. 1B). From the detected photon number, we could infer the bright-state population N_\uparrow , which is equivalent to a projective measurement of $\hat{S}_z = \hat{N}_\uparrow - (N/2)$, where \hat{S}_z is the z component of the collective spin vector

$$\mathbf{S} = \frac{1}{2} \sum_i^N (\hat{\sigma}_i^x, \hat{\sigma}_i^y, \hat{\sigma}_i^z) \quad (6)$$

By performing a final global rotation before measuring, we could measure the moments of any component of \mathbf{S} . The directly observed variance of the measurement $(\Delta S_z)^2$ is well described by the sum of two noise terms: spin noise $(\Delta S_z^s)^2$ and photon shot noise $(\Delta S_{\text{psn}})^2$. Here, ΔX indicates the standard deviation of repeated measurements of \hat{X} . In this paper, we use the underlying spin noise $(\Delta S_z^s)^2 = (\Delta S_z)^2 - (\Delta S_{\text{psn}})^2$ for comparison with theory predictions, but use the directly

observed variance in the measurement $(\Delta S_z)^2$ for evaluating the spin-squeezing entanglement witness. The ratio $(\Delta S_{\text{psn}})^2/(\Delta S_z^s)^2$ is typically 0.13 (−8.8 dB), so the noise subtraction is small for all but the most squeezed states observed here. Other sources of state readout noise are not appreciable (28).

The depolarization of the collective spin length $|\langle \mathbf{S} \rangle|$, or contrast, caused by the Ising interaction is a canonical example of non-equilibrium quantum dynamics (30–33). Quantum correlations reduce the contrast and cause the collective spin state to wrap around the Bloch sphere that represents the state space (Fig. 2A). However, the contrast also decreases from decoherence, which destroys correlations, effectively shrinking the Bloch sphere. Our calculation accounts for both effects; for homogeneous Ising interactions $J_{i,j} = \bar{J}$ and at the time scales explored experimentally, the contrast is approximately (28) given by

$$|\mathbf{S}| \approx \exp(-\Gamma\tau) \frac{N}{2} \left[\cos\left(\frac{2\bar{J}\tau}{N}\right) \right]^{N-1} \quad (7)$$

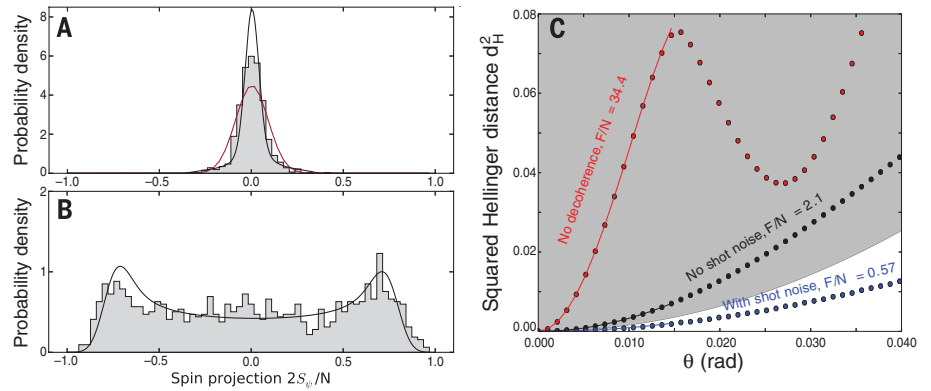
where τ is the total ODF interaction time (Fig. 1C) and Γ is the total single-particle decoherence rate (28) due to spontaneous emission from the ODF lasers.

We show the depolarization dynamics of $|\langle \mathbf{S} \rangle|$ in our experiment in Fig. 2B, distinguishing effects of coherent interactions from decoherence. We determined $|\langle \mathbf{S} \rangle|$ from measurements of $\langle \hat{S}_x \rangle$, performing independent experiments to confirm that $\langle \hat{S}_y \rangle = \langle \hat{S}_z \rangle = 0$ after evolution under \hat{H}_I . To distinguish the depolarization caused only by decoherence associated with the ODF lasers, we performed experiments at $\delta = +2\pi \times 50$ kHz, effectively eliminating the Ising coupling while leaving the spontaneous emission rate unchanged. The dashed line in Fig. 2B is a fit to the observed

Fig. 4. Full counting statistics of a non-Gaussian spin state and theoretical Fisher information.

(A and B) Histograms showing the squeezed (A) and antisqueezed (B) quadratures of the collective spin of $N = 127 \pm 4$ ions, corresponding to $\psi = 5.4^\circ$ and $\psi = 92^\circ$, respectively; $\tau = 3$ ms. The integral of the histogram is normalized to unity. The red line is the Gaussian distribution of the initial, unsqueezed state. The solid black line is the probability density predicted from numerical calculations (28), assuming homogeneous interactions and including decoherence from spontaneous emission and magnetic field fluctuations. We account for photon shot noise by convolving the theoretical probability density with a Gaussian distribution with a variance $(\Delta S_{\text{psn}})^2/(N/4)$.

(C) Extraction of the Fisher information from the theoretically computed Hellinger distance without (black) and with (blue) photon shot noise, including the effects of decoherence from spontaneous emission and magnetic field noise. Shown in red is the Hellinger distance in the absence of decoherence or photon shot noise, for comparison. The points denote computed values of the Hellinger distance; the lines are small-angle quartic fits. The gray swath denotes the region of entangled states (28).



exponential decay, measuring Γ in our system (28). The faster contrast decay for μ tuned near ω_z is in good agreement with Eq. 7 for a range of system sizes. For these data, $\delta = 4\pi/\tau$, ensuring spin-motion decoupling of the COM mode at the end of the experiment (25). The collapse of the data to a single curve when plotted as a function of $2\bar{J}\tau/\sqrt{N}$ (Fig. 2B, inset) provides strong evidence that the depolarization is primarily the result of spin-spin interactions. However, depolarization dynamics alone are not enough to prove that entanglement exists in the ensemble.

To verify entanglement, we used the Ramsey squeezing parameter ξ_R^2 , which only requires measuring the variance of collective observables, instead of full state tomography. The Ramsey squeezing parameter is

$$\xi_R^2 = N \frac{\min_{\psi} [(\Delta S_{\psi})^2]}{|\langle S \rangle|^2} \quad (8)$$

where

$$\hat{S}_{\psi} = \frac{1}{2} \sum_i^N \cos(\psi) \hat{\sigma}_i^z + \sin(\psi) \hat{\sigma}_i^y \quad (9)$$

and \min_{ψ} indicates taking the minimum as a function of ψ . For an unentangled spin state, polarized along the x axis, $|\langle S \rangle| = N/2$ and the spin noise is set by Heisenberg uncertainty relations to $(\Delta S_y)^2 = (\Delta S_z)^2 = N/4$, so $\xi_R^2 = 1$. This quantum noise limits the signal-to-noise ratio for a wide range of quantum sensors based on ensembles of independent quantum objects (34). Nonclassical correlations can redistribute quantum noise between two orthogonal quadratures of the collective spin, squeezing the noise such that $(\Delta S_{\psi})^2 < N/4$ and $\xi_R^2 < 1$. These squeezed states are entangled (35), and furthermore, $\xi_R^2 < 1$ proves that the entangled state is a useful resource for precision sensing (15, 34–43).

At short times, the non-equilibrium spin dynamics caused by the Ising interaction can produce spin-squeezed states (15, 32, 34, 44). Figure 3, A and B, shows the measured time evolution of the spin variance $(\Delta S_{\psi})^2$ of 86 ions, normalized to the spin variance of the initial, unentangled

state. We compared the data to an analytic model (32) that assumes homogeneous Ising interactions and fully accounts for both elastic and spin-changing spontaneous emission. The data clearly show the development of squeezed and anti-squeezed quadratures, and deviations from perfectly coherent Ising dynamics are well described by the effects of spontaneous emission alone. Similar data for different values of N are shown in (28).

Using measurements of the directly observed spin variance $(\Delta S_{\psi})^2$ and contrast $|\langle S \rangle|$, we obtained ξ_R^2 for a range of values of τ . As shown by a plot of the minimum observed ξ_R^2 for each N in Fig. 3C, the entanglement witness $\xi_R^2 < 1$ is satisfied for seven independent data sets with N ranging from 21 to 219. We observe a minimum $\xi_R^2 = -4.0 \pm 0.9$ dB for $N = 84$ ions. We also show ξ_R^2 measured for the initial state, confirming our calibration of N . For comparison, Fig. 3C shows the absolute minimum ξ_R^2 predicted for coherent Ising interactions. The majority of the observed discrepancy for ensembles ranging from 60 to 150 ions is accounted for by photon shot noise, spontaneous emission, and the finite sampling of τ and ψ . For other ion numbers (28), we still observe good agreement in the antisqueezed spin variance, but the minimum spin variance and ξ_R^2 deviate further from the prediction. We attribute the deviation to technical noise sources (28).

The Ramsey squeezing parameter is an effective entanglement witness at short times when quantum noise is approximately Gaussian. At longer times, the growth of spin correlations causes both the depolarization seen in Fig. 2 and the increase in $\min_{\psi} [(\Delta S_{\psi})^2]$, due to the appearance of non-Gaussian quantum noise in the collective spin. Both effects cause ξ_R^2 to increase above 1, which we call an oversqueezed state. Oversqueezed states can be entangled (45); however, ξ_R^2 can also increase simply because of decoherence.

Signatures of quantum correlations at longer interaction times are seen in a histogram of the measurements of $\langle \hat{S}_{\psi} \rangle$ for an oversqueezed state

of 127 ions after an interaction time of $\tau = 3$ ms (Fig. 4B). For times well beyond the optimum squeezing time, we see a clear non-Gaussian distribution for the antisqueezed quadrature. The distribution for $\psi = 5.4^\circ$ (Fig. 4A) also contains non-Gaussian characteristics in the tails away from the narrow central feature. We found good agreement between these data and a theoretical model of the full counting statistics. Even though $\xi_R^2 = 26$, the theoretically predicted state is entangled, as shown by an entanglement witness based on the Fisher information F (Fig. 4C). The quantum Fisher information has been used as an entanglement witness in other trapped-ion simulators (46). Here, we bound the value of F using the approach in (40) and find $F/N > 2.1$, which satisfies the inequality of the entanglement witness $F/N > 1$ (45). Photon shot noise in our measurement limits our capability to directly witness the entanglement experimentally (28), but the good agreement with theory indicates that the state of the ensemble is consistent with an entangled, oversqueezed state. Additionally, we experimentally confirmed that this procedure for bounding F witnesses entanglement of squeezed states (fig. S11). The full counting statistics are only efficiently computable for homogeneous couplings, a good approximation for the small detunings δ considered here. For future work with inhomogeneous Ising coupling, obtaining the full counting statistics theoretically will likely be intractable for more than 20 to 30 spins.

The techniques presented here are applicable to precision sensors using trapped ions, where the number of ions is limited by systematic errors arising from ion motion (47), and could be useful for quantum-enhanced metrology with non-Gaussian spin states (40, 48–50). These results benchmark controlled quantum evolution in a 2D platform with more than 200 spins, establishing a foundation for future experiments studying the full transverse-field Ising model in regimes inaccessible to classical computation. With the implementation of single-spin readout, the simulator could provide unique opportunities to study the dynamics of spin correlations in 2D systems,

such as Lieb-Robinson bounds (19) and many-body localization in the presence of disorder (5, 6).

REFERENCES AND NOTES

1. R. P. Feynman, *Int. J. Theor. Phys.* **21**, 467–488 (1982).
2. P. Hauke, F. M. Cucchietti, L. Tagliacozzo, I. Deutsch, M. Lewenstein, *Rep. Prog. Phys.* **75**, 082401 (2012).
3. I. M. Georgescu, S. Ashhab, F. Nori, *Rev. Mod. Phys.* **86**, 153–185 (2014).
4. R. J. Elliott, P. Pfeuty, C. Wood, *Phys. Rev. Lett.* **25**, 443–446 (1970).
5. K. Binder, A. P. Young, *Rev. Mod. Phys.* **58**, 801–976 (1986).
6. R. Nandkishore, D. A. Huse, *Annu. Rev. Condens. Matter Phys.* **6**, 15–38 (2015).
7. D. Belitz, T. R. Kirkpatrick, T. Vojta, *Rev. Mod. Phys.* **77**, 579–632 (2005).
8. S. Sachdev, *Quantum Phase Transitions* (Wiley, 2007).
9. T. F. Ronnow et al., *Science* **345**, 420–424 (2014).
10. A. Lucas, *Front. Phys.* **2**, 5 (2014).
11. J. Simon et al., *Nature* **472**, 307–312 (2011).
12. A. de Paz et al., *Phys. Rev. Lett.* **111**, 185305 (2013).
13. T. Fukuhara et al., *Phys. Rev. Lett.* **115**, 035302 (2015).
14. R. C. Brown et al., *Science* **348**, 540–544 (2015).
15. I. D. Leroux, M. H. Schleier-Smith, V. Vuletić, *Phys. Rev. Lett.* **104**, 073602 (2010).
16. B. Yan et al., *Nature* **501**, 521–525 (2013).
17. D. Porras, J. I. Cirac, *Phys. Rev. Lett.* **92**, 207901 (2004).
18. P. Jurcevic et al., *Nature* **511**, 202–205 (2014).
19. P. Richerme et al., *Nature* **511**, 198–201 (2014).
20. R. Islam et al., *Science* **340**, 583–587 (2013).
21. R. Schmied, J. H. Wesenberg, D. Leibfried, *Phys. Rev. Lett.* **102**, 233002 (2009).
22. C. D. Bruzewicz, R. McConnell, J. Chiaverini, J. M. Sage, <http://arxiv.org/abs/1511.03293> (2015).
23. J. D. Balmtrusch, A. Negretti, J. M. Taylor, T. Calarco, *Phys. Rev. A* **83**, 042319 (2011).
24. J. W. Britton et al., *Nature* **484**, 489–492 (2012).
25. B. C. Sawyer et al., *Phys. Rev. Lett.* **108**, 213003 (2012).
26. C.-C. J. Wang, A. C. Keith, J. K. Freericks, *Phys. Rev. A* **87**, 013422 (2013).
27. M. J. Biercuk et al., *Quantum Inf. Comput.* **9**, 920–949 (2009).
28. See supplementary materials on Science Online.
29. D. Leibfried et al., *Nature* **422**, 412–415 (2003).
30. M. Kastner, *Phys. Rev. Lett.* **106**, 130601 (2011).
31. M. V. D. Worm, B. C. Sawyer, J. J. Bollinger, M. Kastner, *New J. Phys.* **15**, 083007 (2013).
32. M. Foss-Feig, K. R. A. Hazzard, J. J. Bollinger, A. M. Rey, *Phys. Rev. A* **87**, 042101 (2013).
33. K. R. A. Hazzard et al., *Phys. Rev. A* **90**, 063622 (2014).
34. D. Wineland, J. Bollinger, W. Itano, F. Moore, D. J. Heinzen, *Phys. Rev. A* **46**, R6797 (1992).
35. A. Sørensen, L. M. Duan, J. I. Cirac, P. Zoller, *Nature* **409**, 63–66 (2001).
36. L. K. Shalm, R. B. A. Adamson, A. M. Steinberg, *Nature* **457**, 67–70 (2009).
37. W. Wasilewski et al., *Phys. Rev. Lett.* **104**, 133601 (2010).
38. C. D. Hamley, C. S. Gerving, T. M. Hoang, E. M. Bookjans, M. S. Chapman, *Nat. Phys.* **8**, 305–308 (2012).
39. C. F. Ockeloen, R. Schmied, M. F. Riedel, P. Treutlein, *Phys. Rev. Lett.* **111**, 143001 (2013).
40. H. Strobel et al., *Science* **345**, 424–427 (2014).
41. N. Behbood et al., *Phys. Rev. Lett.* **113**, 093601 (2014).
42. O. Hosten, N. J. Engelsens, R. Krishnakumar, M. A. Kasevich, *Nature* **529**, 505–508 (2016).
43. K. C. Cox, G. P. Greve, J. M. Weiner, J. K. Thompson, *Phys. Rev. Lett.* **116**, 093602 (2016).
44. M. Kitagawa, M. Ueda, *Phys. Rev. A* **47**, 5138–5143 (1993).
45. L. Pezzé, A. Smerzi, *Phys. Rev. Lett.* **102**, 100401 (2009).
46. J. Smith et al., <http://arxiv.org/abs/1508.07026> (2015).
47. K. Arnold et al., *Phys. Rev. A* **92**, 032108 (2015).
48. B. Lücke et al., *Phys. Rev. Lett.* **112**, 155304 (2014).
49. F. Haas, J. Volz, R. Gehr, J. Reichel, J. Estève, *Science* **344**, 180–183 (2014).
50. R. McConnell, H. Zhang, J. Hu, S. Čuk, V. Vuletić, *Nature* **519**, 439–442 (2015).

ACKNOWLEDGMENTS

We thank D. Hume, J. Thompson, A. Keith, J. Schachenmayer, A. Safavi-Naini, M. Gaerttner, and M. Kastner for helpful

discussions. Supported by NSF grant PHY 1521080, JILA-NSF grant PFC-1125844, the Army Research Office, and the Air Force Office of Scientific Research and its Multidisciplinary University Research Initiative (A.M.R.) and by a National Research Council Research Associateship Award at NIST (J.G.B., M.F.-F., and M.L.W.). All authors acknowledge financial support from NIST. This manuscript is the contribution of NIST and is not subject to U.S. copyright.

OPTICAL MATERIALS

A highly efficient directional molecular white-light emitter driven by a continuous-wave laser diode

Nils W. Rosemann,^{1,2} Jens P. Eufner,^{2,3} Andreas Beyer,^{1,2} Stephan W. Koch,^{1,2} Kerstin Volz,^{1,2} Stefanie Dehnen,^{2,3*} Sangam Chatterjee^{1,2,4*}

Tailored light sources have greatly advanced technological and scientific progress by optimizing the emission spectrum or color and the emission characteristics. We demonstrate an efficient spectrally broadband and highly directional warm-white-light emitter based on a nonlinear process driven by a cheap, low-power continuous-wave infrared laser diode. The nonlinear medium is a specially designed amorphous material composed of symmetry-free, diamondoid-like cluster molecules that are readily obtained from ubiquitous resources. The visible part of the spectrum resembles the color of a tungsten-halogen lamp at 2900 kelvin while retaining the superior beam divergence of the driving laser. This approach of functionalizing energy-efficient state-of-the-art semiconductor lasers enables a technology complementary to light-emitting diodes for replacing incandescent white-light emitters in high-brilliance applications.

The impact of well-managed light on our everyday life is immeasurable (1, 2). The light-emitting diode (LED) is one of the most prominent developments since the invention of incandescent lightbulbs in the late 1800s (3). The latter dissipate most energy in the infrared as heat, whereas typical white LEDs cover only the visible spectrum. Most prominent examples of white-light LEDs are based on gallium nitride (4, 5). Their narrow-band ultraviolet (UV) emission is converted into visible light by applying phosphors (6–9). This cold light has tremendous advantages with respect to energy efficiency. Other concepts pursued for efficient white-light generation include the combination of red, green, and blue emitters (10), which is currently the path of choice for organic LEDs (11–14). All types of LEDs excel due to their virtually Lambertian emission patterns that are highly desirable for applications like active displays that require large viewing angles (15). However, this poses challenges in targeted illumination and projection of light due to the associated large etendue $G = A\Omega$, where A is the

source area and Ω is the solid angle of emission (16). Ideally, the etendue remains constant throughout an entire optical system where light undergoes perfect reflections or refractions. It can increase—for example, when impinging on a diffusor—but cannot be decreased without loss in radiance. This renders low-etendue sources extremely desirable for devices requiring high spatial resolution like microscopes or for applications with high throughput, such as projection systems.

Other concepts of white-light generation by monochromatic sources besides phosphors rely on nonlinear effects that provide very broadband supercontinua and are widely used in many scientific applications (17, 18). These are often referred to as brilliant sources. They generally feature small, point-source-like emission areas due to the tightly focused short-pulsed driving lasers that are used to overcome the vast peak electric field strength required to invoke the extremely nonlinear effects such as soliton formation (19). Hence, the related challenges, such as the system size, price, and energy requirements, restrict the use of supercontinuum sources to scientific laboratory use and the medical sector—for example, in coherent anti-Stokes Raman scattering (20) or optical coherence tomography (21), as well as for defense and security applications.

Here, we use a molecule-based solid compound as an extremely nonlinear medium. It enables the steady-state operation of a low-etendue, directional broadband white-light source covering the entire

¹Fachbereich Physik, Philipps-Universität Marburg, DE-35032 Marburg, Germany. ²Wissenschaftliches Zentrum für Materialwissenschaften, Philipps-Universität Marburg, DE-35032 Marburg, Germany. ³Fachbereich Chemie, Philipps-Universität Marburg, DE-35032 Marburg, Germany. ⁴Institute of Experimental Physics I, Justus-Liebig-University, DE-35392 Giessen, Germany.

*Corresponding author. Email: stefanie.dehnen@uni-marburg.de (S.D.); sangam.chatterjee@physik.uni-giessen.de (S.C.)

Quantum spin dynamics and entanglement generation with hundreds of trapped ions

Justin G. Bohnet Brian C. Sawyer Joseph W. Britton Michael L. Wall Ana Maria Rey Michael Foss-Feig John J. Bollinger

Science, 352 (6291), • DOI: 10.1126/science.aad9958

Hundreds of ions simulate magnetism

Strongly interacting quantum systems present a challenge to computational methods even at a relatively low particle number of a few dozen. Researchers are looking to tackle such problems by simulating them in a well-understood and controllable system. A linear array of ions is one such system; however, assembling a large enough number of ions is tricky. Bohnet *et al.* show that a two-dimensional “crystal” of around 200 Be ions held together by magnetic and electric fields in a so-called Penning trap can simulate quantum magnetism. The work sets the stage for simulations with more complicated forms of interaction that classical computers would find intractable.

Science, this issue p. 1297

View the article online

<https://www.science.org/doi/10.1126/science.aad9958>

Permissions

<https://www.science.org/help/reprints-and-permissions>

Use of this article is subject to the [Terms of service](#)